Available online at www.sciencedirect.com
SCIENCE DIRECT®
International Journal of Fatigue 25 (2003) 1135–1145
International Journal of Fatigue
www.elsevier.com/locate/ijfatigue

Microstructural characterisation of fatigue crack initiation in Al-based plain bearing alloys

M.C. Mwanza [a,*], M.R. Joyce [a], K.K. Lee [b], S. Syngellakis [c], P.A.S. Reed [a]

[a] *Materials Research Group, School of Engineering Sciences, University of Southampton, Highfield, Southampton SO17 1BJ, UK*
[b] *ISIS, Electronics and Computer Science, University of Southampton, Highfield, Southampton SO17 1BJ, UK*
[c] *Computational Engineering & Design Group, School of Engineering Sciences, University of Southampton, Highfield, Southampton SO17 1BJ, UK*

Abstract

The fatigue initiation behaviour of two Al-based bearing lining alloys has been assessed by image analysis tessellation techniques and subsequent adaptive numerical classification approaches. Fatigue initiation occurs by decohesion at Si particles, and in the absence of Si particles decohesion occurs at Sn particles. In both cases, relatively unclustered, large particles initiate fatigue, and the relative position of the nearest neighbour particle seems to have significance. This can be explained qualitatively in terms of strain mismatch arising from differing elastic moduli between the particles and surrounding Al matrix and local stress concentration and superposition effects. The lining alloy containing no Si and high Sn content exhibits more directionality, and a heavier dependence on angular information is found by the classifier.

Keywords: Al bearing alloys; Statistical microstructural characterisation; Fatigue crack initiation; Finite body tessellation

1. Introduction

Plain hydrodynamic bearings are used as main and connecting rod big end bearings in internal combustion engines. The trend towards increased specific power output and reduced weight of engines results in an increase in the loading on the bearing, and the potential for fatigue damage is increased. Traditionally, multilayered bearings, "bimetals" or "trimetals", provide the required combination of properties for the bearing; the material systems considered in this work are aluminium bimetals, which comprise a tri-layered structure consisting of a steel backing, a thin pure Al interlayer and a soft, conformable, multiphase Al alloy lining. This tri-layered plain bearing is shown schematically in Fig. 1. In service, the bearing lining is loaded by pressure from the hydrodynamic oil layer causing cyclic stresses in the bearing lining [1]. Fatigue damage is observed in bearing samples run in test rigs under high cyclic stresses, with cracks typically initiating at multiple points on the bearing lining surface. In some cases, this can cause sections of the lining to detach completely [2]. This paper compares the fatigue resistance of two Al alloy plain bearing materials and investigates the role of the lining micro-

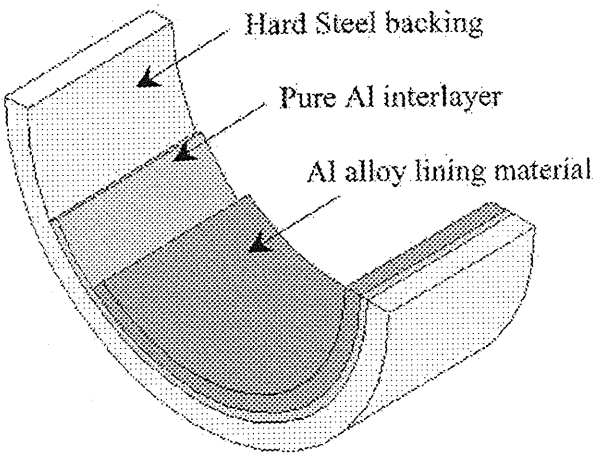

Fig. 1. Half shell schematic of tri-layered plain bearing.

* Corresponding author. Tel.: +44-2380-595096; fax: +44-2380-593016.
E-mail address: m.c.mwanza@soton.ac.uk (M.C. Mwanza).

0142-1123/$ - see front matter © 2003 Elsevier Ltd. All rights reserved.
doi:10.1016/S0142-1123(03)00148-8

structure in the initiation behaviour of the alloys, detailing the identification of initiation sites and the probability that a given site will initiate fatigue cracks.

2. Experimental procedure

2.1. Material characterisation

The two lining materials studied are: an Al–20wt%Sn alloy (Al–20Sn) and an Al–12wt%Sn–4wt%Si alloy (Al–12Sn–4Si). These linings are produced by continuous casting before being cut into billets, and are then extensively cold worked to reduce their thickness. This lining is then roll bonded to the steel backing and annealed before finally being formed into bearings. The lining microstructures of the two bearing systems are shown in Fig. 2 in the as-polished condition. Both alloys are multiphase materials, with the Sn existing as a distinct phase in both systems. In Al–20Sn, the majority of the secondary phase is Sn, with the occasional darker grey phase being identified as $CuAl_2$ intermetallics. In Al–12Sn–4Si, the Si phase occurs as a spheroidal, dark-grey, uniformly distributed phase often associated with, and occasionally entirely encapsulated by, the lighter grey Sn phase.

2.2. Fatigue testing

The specimens used for the fatigue tests were the as-received finished half-shell bearings, and bend-bar type flat strips measuring 80 mm × 20 mm × 2 mm produced in the condition immediately prior to the final bearing forming operation. Both were tested in a three-point bend configuration on a digitally controlled, Instron 8502 servo-hydraulic fatigue-testing machine (±50 kN load capacity). The fatigue test set-up of both of these specimens is shown in Fig. 3. All tests were carried out in air at room temperature, at a load ratio of 0.1 and a frequency of 10 Hz. To obtain the fatigue lifetimes, uninterrupted run out tests were conducted at a range of loads on the finished bearings, whilst interrupted tests involving frequent acetate replication of the polished flat strip bend-bar surface gave detailed records of crack initiation behaviour for a particular stress level. Stress/strain levels for the replication tests were chosen to give appropriate testing lifetimes (<150 000 cycles) to allow the replication process to be used within reasonable testing times. An elasto-plastic finite element (FE) model [3] was used to calculate the maximum lining surface stresses in both the bearing and the flat strip. This assimilates the complex test geometry and makes use of simple isotropic multilinear hardening curves to represent each material layer. Both alloys were tested with loads such that the nominal lining surface stress was 105 MPa. Comparison uninterrupted tests were carried out on the flat strips to assess the effect, if any, of the replication process on fatigue performance. Flat strip samples were used for acetate replication due to the difficulties of obtaining a high quality polish on the curved lining of a finished bearing. A bearing sample was considered to have failed when it had deformed by 0.3 mm from its maximum deflection under maximum load, and by 0.5 mm in the case of the flat strip. These differing criteria were required to produce qualitatively similar amounts of damage in the two testing geometries. Post-test acetate replicas and failed samples were examined using optical and SEM microscopy to unambiguously identify the crack initiation sites.

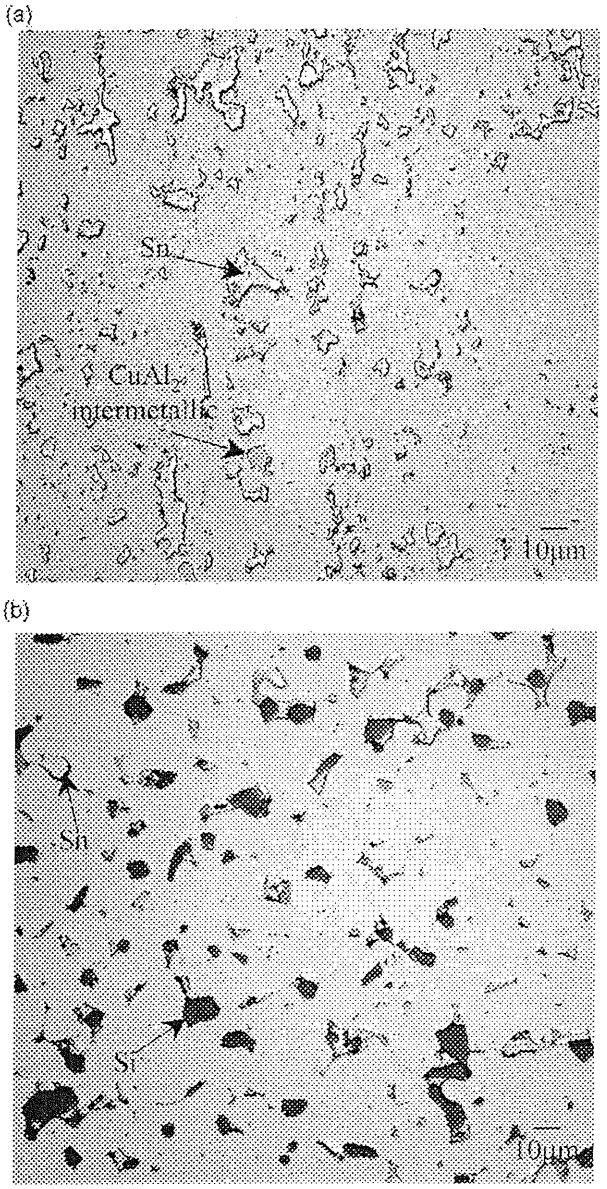

Fig. 2. Micrograph of unetched sections of (a) Al–20Sn and (b) Al–12Sn–4Si lining material.

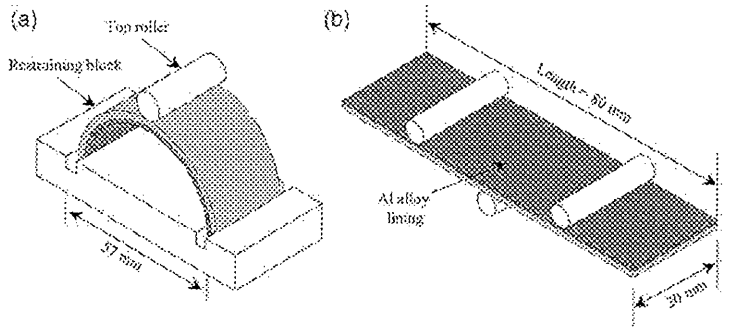

Fig. 3. Three point bend set-up for (a) half shell bearings and (b) flat strip sections.

3. Fatigue test results

3.1. Bearing results

Using the σ/ε results calculated for each lining by the FE model described above [3], fatigue data were collated for the two bearings. For the lifetime characterisation, a strain–life methodology was adopted since it accounted for the considerable plastic deformation occurring within the lining. Fig. 4 shows the plastic strain amplitude ($\Delta\varepsilon_p/2$) vs. lifetime (N) curves of the Al–20Sn and Al–12Sn–4Si bearings in ambient conditions. It is seen that the number of cycles to failure (N_f) in the Al–12Sn–4Si bearing is higher than that of the Al–20Sn bearing for the same calculated $\Delta\varepsilon_p/2$, with larger variations in N_f at higher $\Delta\varepsilon_p/2$ and a more comparable behaviour at the lower strain levels, more comparable to service conditions. The FE modelling showed that the lining behaved plastically at stresses in excess of its yield stress and that for a considerable proportion of the load ($L_{max} > 2$ kN), the steel backing adjacent to the lining was also in excess of its yield stress. This suggests that as part of a bearing system, both the Al–12Sn–4Si and Al–20Sn linings can apparently tolerate cyclic stresses in excess of the yield stress, with the Al–12Sn–4Si outperforming the Al–20Sn.

3.2. Flat strip results

Fig. 5 compares the bearing and flat strip results for both alloys. The lifetimes for the flat strips correlate well with the band of behaviour defined by the bearings at the same $\Delta\varepsilon_p/2$ for both alloys. The number of cycles to failure (N_f) in the Al–12Sn–4Si flat strip is higher than that of the Al–20Sn lining, for the same $\Delta\varepsilon_p/2$, again suggesting a greater fatigue resistance in the Al–12Sn–4Si lining than in the Al–20Sn. The comparison uninterrupted tests showed a minimal effect of the replication process on the fatigue performance of both alloys.

4. Critical microstructural features for fatigue crack initiation

Fatigue crack initiation in both alloys was seen to be associated with decohesion of second phase particles from the surrounding matrix. In Al–20Sn, these particles were predominantly Sn, but occasionally intermetallics, whilst in Al–12Sn–4Si, fatigue crack initiation was exclusively associated with the Si phase [4]. Fig. 6 shows examples of crack initiation in both alloys. In order to assess any critical features, the set of particles

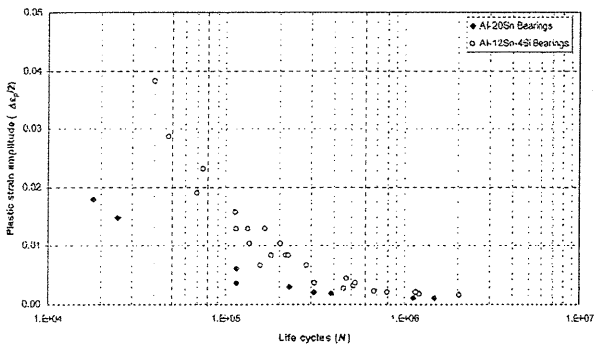

Fig. 4. Fatigue life of Al–20Sn and Al–12Sn–4Si bearings.

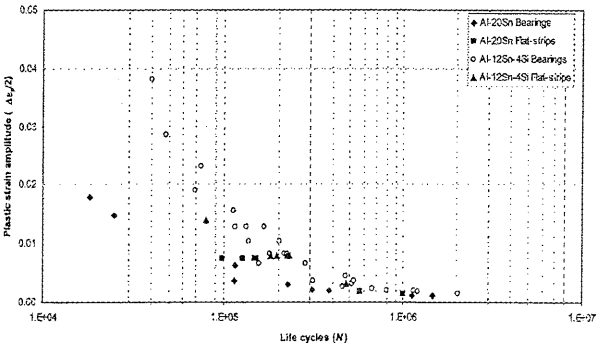

Fig. 5. Fatigue life of Al–20Sn and Al–12Sn–4Si flat strips and bearings.

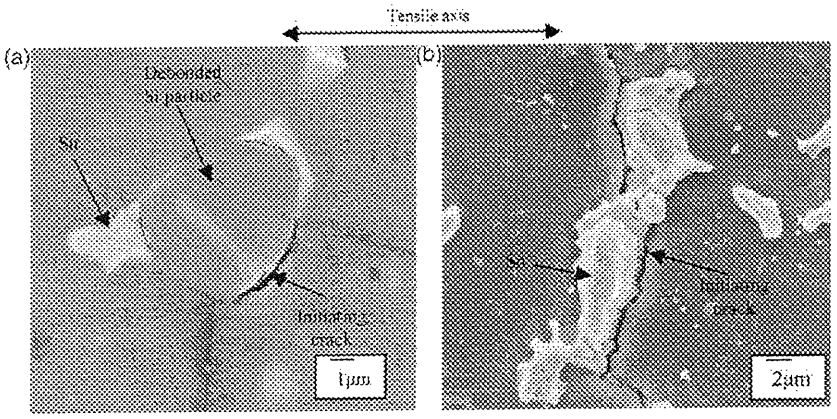

Fig. 6. FEGSEM micrographs showing typical fatigue initiation site in (a) a debonded Si phase in Al–12–Sn–4Si, and (b) a Sn/matrix interface in Al–20Sn.

causing fatigue crack initiation were statistically compared with the general particle population.

To assess the distribution of these secondary phases, a statistical particle assessment based on finite body tessellation (FBT), developed by Boselli et al. [5], was used. This tessellation approach provides a means of statistically characterising a multiphase microstructure by generating a series of tessellated cells surrounding each particle in the microstructure such that all points within a given cell are closer to the enclosed particle than to any other. It is this ability of measuring parameters on a "cell by cell" basis that enables the characterisation of fatigue initiating particles The 11 FBT feature measurements generated for cell-based and near-neighbour parameters are illustrated in Fig. 7 and are defined thus: (i) object area (OA), (ii) object aspect ratio (O.Asp.Rat) = maximum chord length divided by maximum perpendicular width, (iii) object angle (O.Ang) = angle of the objects longest chord with respect to the horizontal (where $0 \leq \theta \leq \pi/2$ rad), (iv) cell area (CA), (v) cell aspect ratio (C.Asp.Rat), (vi) cell angle (C.Ang) = angle of the cell's longest chord with respect to the horizontal, (vii) local area fraction (LAF) = OA/CA × 100, (viii) number of near neighbours (NNN) = number of neighbours sharing a cell boundary with object of interest, (ix) nearest neighbour distance (d_{min}) = shortest interfacial distance with any of the near neighbours, (x) mean near neighbour distance (d_{mean}) = average of interfacial distances to all of the near neighbours, and (xi) nearest neighbour angle (N.N.Ang) = angle of line joining centroid of object to centroid of nearest neighbour. Unlike the classical Dirichlet tessellation method, based on particle centroids, which can produce cell/particle overlaps for particles with a wide size range or high aspect ratios, the FBT technique is capable of generating representative tessellated structures even for large or elongated particles, producing cells that are far more representative of the global area within which the included particles may be expected to lie.

This analysis was restricted to the Sn phase in Al–20Sn and to the Si phase in Al–12Sn–4Si. For the Al–

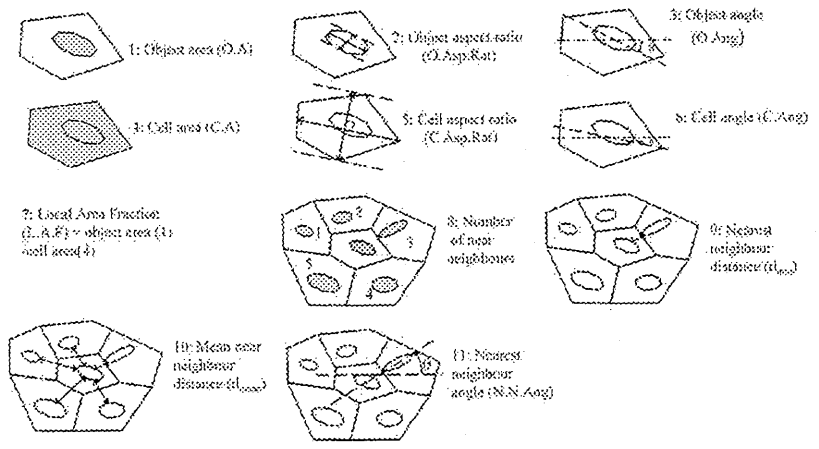

Fig. 7. The 11 feature measurements obtained by FBT

20Sn, five regions of microstructure were randomly selected and binary images of the Sn secondary phases produced, each containing approximately 400 secondary Sn particles. In the Al–12Sn–4Si, 10 regions of microstructure were randomly selected, each containing approximately 300 discrete Si secondary phases. The cells produced by the tessellation were divided into three populations according to the role that the enclosed secondary particle played in crack initiation: (i) initiating cells—cells containing a particle initiating a crack; (ii) bordering cells—cells sharing a common boundary with an initiating cell (nearest neighbour of particle causing initiation); (iii) background cells—cells neither containing nor sharing a boundary with an initiating cell.

Fig. 8 shows a typical tessellated binary image of the Al–20Sn Sn phase with the above cell classification and tensile axis direction. The mean values and standard deviations for the measurements made in each population for both alloys are shown in Table 1. In both cases, the mean object area (OA = Si or Sn particle size) of the initiating particles is considerably higher than that of the bordering cells, and this in turn is higher than that of the background cells. Similar observations were made for CA and LAF, where again initiating particles had larger values in both alloys. Two other trends are clearly discernable. Firstly, in the Al–20Sn, the initiating population shows a distinct shift in the angular parameters (O.Ang, C.Ang and N.N.Ang) towards higher values; this is not seen in the Al–12Sn–4Si, where the particles appear to be more randomly orientated. This alignment result in the Al–20Sn is attributed to the rolling process during manufacture. Secondly, when the statistical data are analysed on a particle by particle basis (as opposed to mean values), the frequency distribution of the initiating population in both alloys shows a clear shift towards

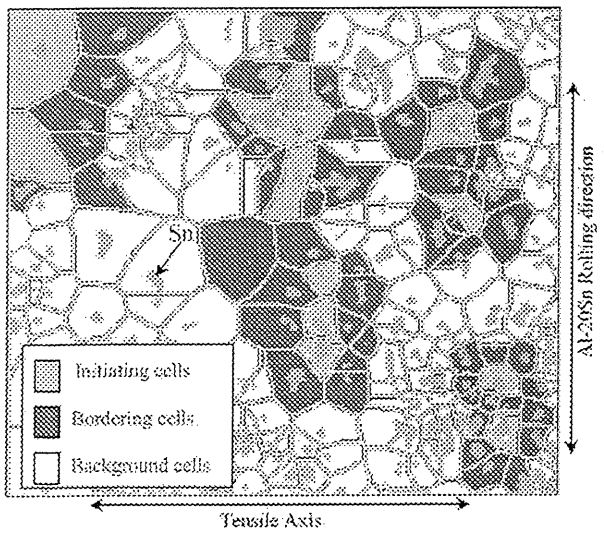

Fig. 8. Al-20Sn tesselated binary showing initiating, bordering and background cells.

higher values for d_{mean}. This indicates that the Si phases associated with fatigue crack initiation are generally more remote from their immediate neighbours.

For the other FBT parameters, however (Asp.Rat etc.), no immediately discernible differences were seen in both alloys, other than greater scatter in the initiation cell distribution probably caused by the small number of initiating cells compared to the other two populations. The large scatter for all the above FBT parameters means that prediction of which particles would initiate failure is not possible by simply considering these individual parameters. It is important to know which combination of these parameters leads to initiation, and with 11 features, considering all possible combinations by inspection is not feasible. Statistical classification techniques that consider all possible combinations of these FBT parameters are more appropriate. The classification approach adopted here uses a modified adaptive numerical modelling (ANM) approach, based on support vector machines with a parsimonious analysis of variance (ANOVA) representation (SUPANOVA) [6]. This classification approach has recently been successfully adopted in considering fatigue initiating features in ADI [7].

4.1. Classification approach using SUPANOVA

Unlike many classification techniques, which place an emphasis on obtaining a good classification rate (e.g. 100% successful classification of those particles associated with crack initiation), the SUPANOVA approach also provides enhanced model transparency and hence aids model interpretation (e.g. why do these particles cause initiation?). Such interpretation provides a valuable mechanistic insight and allows physically based optimisation of the process in question. In applying the SUPANOVA classification, the initiating, bordering and background classes are used. However, since the background and bordering populations are essentially similar, these two populations can be combined. In the Al–20Sn, this reclassification provides two populations, one of 90 phases associated with crack initiation termed the "crack class", and a bordering + background population of 1550 non-initiating phases known as the "non-crack class". For the Al–12Sn–4Si, the crack class comprises 163 phases, while the non-crack class has 2775 phases. Since the two classes are an imbalanced data set (e.g. 90 for "crack" and 1550 for "non-crack" in Al–20Sn), the SUPANOVA classification avoids a bias operating for the more heavily represented class by use of differing misclassification costs and a geometric mean (G_{mean}), which favours a balanced classification by measuring the square root of the product of the class classification rates. A more detailed description of the approach taken to incorporate the differing misclassification costs and performance criteria for imbalanced data can be found in

Table 1
Al–20Sn (Sn) and Al–12Si–4Sn (Si) mean values and standard deviations of FBT parameters on initiating, bordering and background cells

Population	Object area (OA/μm²)		O.Asp.Rat		Object angles (O.Ang/rad)		Cell area (CA/μm²)		C.Asp.Rat		Cell angle (C.Ang/rad)		Local area fraction (LAF)		N.N.N		d_{min} (μm)		d_{mean} (μm)		N.N.Ang (rad)	
	Al–20Sn	Al–12Sn–4Si	Al–20Sn	Al–12Sn–4Si	Al–20Sn	Al–12Sn–4Si	Al–20Sn	Al–12Sn–4Si	Al–20Sn	Al–12Sn–4Si	Al–20Sn	Al–12Sn–4Si	Al–20Sn	Al–12Sn–4Si	Al–20Sn	Al–12Sn–4Si	Al–20Sn	Al–12Sn–4Si	Al–20Sn	Al–12Sn–4Si	Al–20Sn	Al–12Sn–4Si
Overall	57.1 ± 79.4	7.2 ± 6.1	1.6 ± 0.4	1.6 ± 0.5	1.01 ± 0.39	0.99 ± 0.36	612.2 ± 445.9	108.5 ± 70.0	1.6 ± 0.6	1.7 ± 2.9	0.78 ± 0.43	0.79 ± 0.45	9.2 ± 6.7	7.6 ± 5.7	5.5 ± 1.5	5.6 ± 1.5	4.7 ± 4.2	2.2 ± 2.1	16.7 ± 7.6	8.1 ± 3.3	0.92 ± 0.44	0.94 ± 0.45
Initiation	102.6 ± 100.0	12.2 ± 11.5	1.8 ± 0.4	1.5 ± 0.4	1.26 ± 0.22	0.90 ± 0.41	900.1 ± 654	113.6 ± 58.6	1.4 ± 0.3	1.5 ± 0.4	0.93 ± 0.29	0.88 ± 0.42	12.3 ± 8.9	10.5 ± 6.4	5.9 ± 1.3	6.4 ± 1.4	5.3 ± 4.2	2.6 ± 1.9	18.3 ± 6.8	7.6 ± 2.5	1.14 ± 0.41	0.73 ± 0.44
Bordering	89.5 ± 134.2	6.2 ± 6.7	1.7 ± 0.5	1.5 ± 0.4	0.97 ± 0.36	0.88 ± 0.42	750.2 ± 488.6	87.6 ± 53.5	1.5 ± 0.4	1.6 ± 1.2	0.75 ± 0.42	0.79 ± 0.44	10.8 ± 8.3	7.0 ± 5.3	5.8 ± 1.6	6.0 ± 1.4	5.3 ± 4.4	2.5 ± 1.9	17.8 ± 7.4	7.3 ± 2.6	0.96 ± 0.45	0.79 ± 0.46
Back-ground	47.3 ± 56.9	4.2 ± 5.2	1.6 ± 0.4	1.5 ± 0.5	1.0 ± 0.4	0.87 ± 0.4	563.7 ± 407	62.5 ± 43.2	1.6 ± 0.6	1.7 ± 1.5	0.78 ± 0.44	0.77 ± 0.44	8.6 ± 6.1	6.9 ± 5.7	5.4 ± 1.5	5.5 ± 1.4	4.6 ± 4.1	1.9 ± 1.7	16.4 ± 7.7	6.03 ± 2.6	0.89 ± 0.44	0.83 ± 0.45

Lee et al. [8]. The stages in the SUPANOVA classification are briefly detailed below.

4.2. Application of the SUPANOVA classification

From the FBT results, the 11 input parameters (OA, CA, etc.) were normalised between zero and one to avoid bias for any particular feature. For the Al–20Sn, the data were then partitioned into training (30%) and testing (70%) data sets. For the Al–12Sn–4Si, the training data set comprised 45% of the entire particle population, the rest being used for testing. The misclassification costs for each class were then tuned to obtain a good classification performance (based on G_{mean} of the unseen test data) using the pure SVM approach. This partitioning of the data was repeated 10 times with random selection of the training and testing data split each time, thus providing 10 models. The SVM classification has no inherent transparency, and so the sparse ANOVA decomposition is next obtained for each model. The full ANOVA decomposition of the 11 tessellation features has 2048 possible terms (2^{11}), but by using the sparse representation approach adopted in SUPANOVA it was possible to reduce these terms without greatly compromising overall performance. Figs. 9(a–e) and 10(a–j) show examples for both alloys of the relationships found between these input terms (x-axis or x–y axes) and the likelihood of cracking (output on the y- or z-axis) in which a decreasing trend in the y-axis (2D) or the z-axis (3D) indicates increased likelihood of fatigue crack initiation. In Al–12Sn–4Si, the 2048 terms were reduced to just six terms, with the sparse model giving a successful "crack" classification rate of 69%, a successful "non-crack" classification rate of 71% and an overall classification performance based on mean and variance values of G_{mean} = 70% and 1.36%, respectively. In Al–20Sn, the 2048 terms were reduced to 10 terms, with the models giving a successful "crack" classification rate of 58%, a successful "non-crack" classification rate of 64% and an overall mean and variance value of G_{mean} = 60% and 0.55%, respectively. For the Al–20Sn and Al–12Sn–4Si alloys, the univariate (uv), bivariate (bv) and trivariate (tv) terms selected most consistently ($\geq$5/10 times) for the different data-set sampling runs are briefly summarised in Tables 2 and 3.

4.2.1. Selected features in Al–12Sn–4Si

For the Al–12Sn–4Si alloy, Fig. 9(a) shows that the first term picked is the uv relating increasing CA with the increasing likelihood of a Si particle initiating a crack. The increasing probability of a Si particle initiating a crack with increasing LAF is another uv picked up by the classifier (Fig. 9(b)). The fact that increasing CA and increasing LAF (which implies increasing OA since LAF = OA/CA) are picked by the classifier, and not OA alone, is unexpected. Results from the other terms picked (terms 3 and 4) suggest that the orientation of the object (low O.Ang), the cell angle (low C.Ang) and the greater average distance from near neighbours (high d_{mean}) also promote crack initiation. From the uv in the Al-12Sn-4Si system, it is concluded that large Si particles of high LAF are predominantly acting as fatigue initiation sites. The angular information is addressed by term 4, the bv of C.Ang and O.Ang (these terms may be correlated), and term 5, the tv of O.Ang, d_{min} and N.N.Ang. The predictions of these terms, shown in Fig. 9(c, d and e), may be interpreted as: fatigue initiation is likely when C.Ang and O.Ang are low (i.e. when the Si particle major axis is aligned along the tensile axis), except when d_{min} is high and N.N.Ang is low. The selection of d_{min} and N.N.Ang indicates that the position of the nearest neighbour may be significant in determining the behaviour of the central particle.

4.2.2. Selected features in Al–20Sn

In the Al–20Sn classification (Fig. 10(a–j)), term 1 is a uv relationship between increasing O.Ang and the increasing likelihood of the Sn particle initiating a crack. Other uv terms showed that increasing C.Ang and increasing C.Asp.Rat gave increasing likelihood of a particle not initiating a crack. The prediction from these uv terms may be interpreted as: particles aligned perpendicular to the tensile axis (increasing O.Ang) predominantly act as fatigue initiation sites except when the C.Ang or aspect ratios are high. The bv relationships (shown in Fig. 10(d–j)) predict the likelihood of crack initiation based on the combination of the angular information (C.Ang, N.N.Ang, etc.), spatial distributions (mean near neighbour distance (d_{mean})) and the cell-based measurements (LAF). From terms 4 and 5, it is seen that fatigue initiation is more likely to occur when the O.Ang increases with increasing O.Asp.Rat or increasing LAF, respectively. Terms 6–8 also show that increasing N.N.Ang is likely to cause initiation with increasing OA, increasing LAF or increasing C.Ang. It thus appears that if the nearest neighbour is perpendicularly aligned above or below the central Sn particle, crack initiation on the central Sn is likely. These bv relations may be interpreted as: large Sn particles (high OA) with their major axis perpendicular to the tensile axis (high O.Ang) and having their near neighbours in the same alignment as their major axis (high N.N.Ang) are more likely to cause initiation. Term 9 shows that crack initiation is likely with increasing C.Ang and increasing d_{mean}. A high d_{mean} is considered to indicate a relatively unclustered local microstructure. A high d_{mean} for an initiating particle indicates a greater distance generally to the near neighbours for that initiating particle, implying that the spatial distribution of the near neighbours is significant in affecting the local stress distribution around a central Sn particle and causing crack initiation.

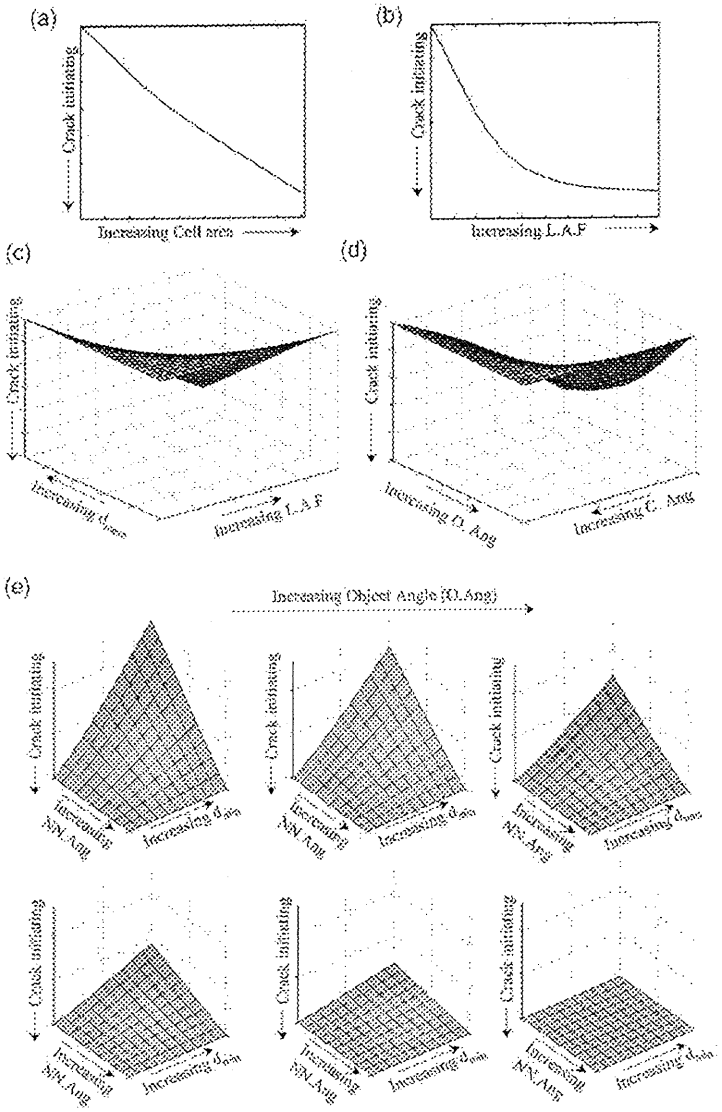

Fig. 9. ANM terms 1 to 5 for Al–12Sn–4Si alloy.

4.2.3. Summary

Deductions from the Al–12Sn–4Si ANM modelling indicate that Si particles associated with fatigue crack initiation are larger than average and have their major axis aligned parallel to the tensile axis. It also seems that fatigue cracks initiate at particles in relatively unclustered areas of local microstructure, where the position of the nearest neighbour may more strongly affect the behaviour of the central particle. In the Al–20Sn, the overall interpretations from the classification are that Sn particles associated with fatigue crack initiations are larger than average, with a high aspect ratio, have their major axis aligned perpendicular to the tensile axis and lie further away from their near neighbours. The effect of the angular position of the nearest neighbour is currently ambiguous, indicating different effects when N.N.Angles are combined with different parameters.

5. Discussion

Some of the uv components (e.g. O.Ang and C.Asp.Rat) identified by the SUPANOVA classification could also be seen as important when simply comparing mean values between initiating and non-initiating particles (Table 1). With SUPANOVA, however, we are also able to pick up higher order interactions that are not easily identifiable by simple means of visualisation as well as achieve good prediction rates. The SUPANOVA classifier can also be used to assess the likelihood of

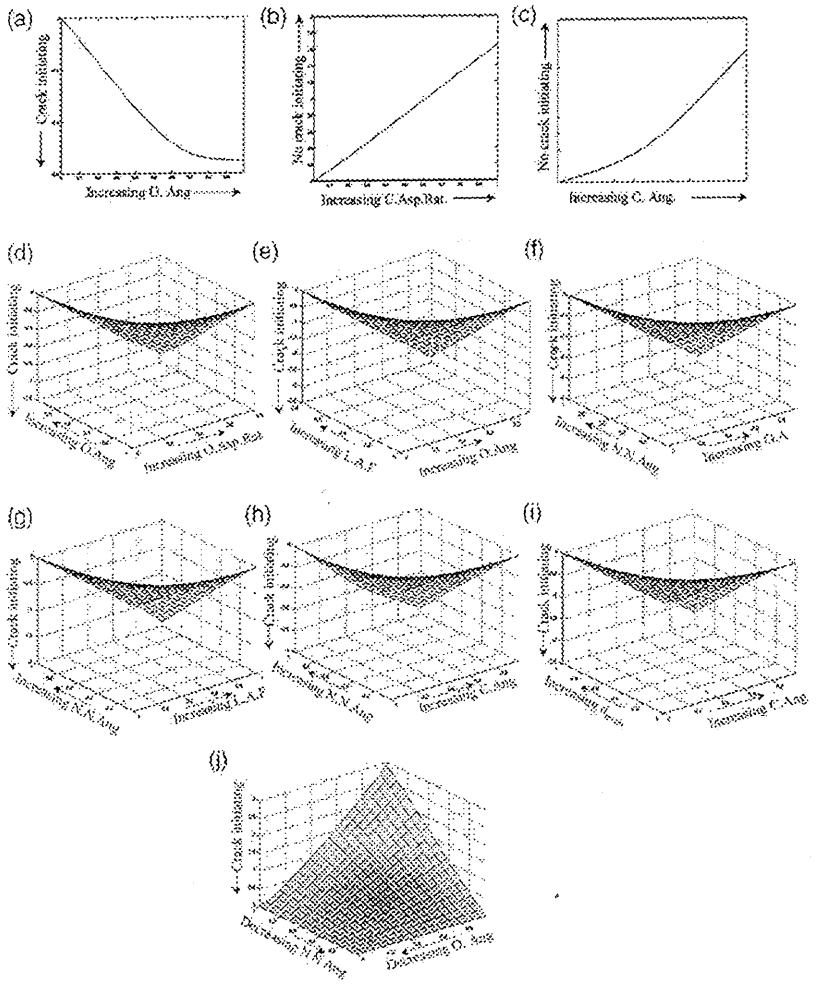

Fig. 10. ANM terms 1 to 10 for Al–20Sn alloy.

Table 2
Al–12Sn–4Si SUPANOVA terms selected (and the components thereof) and their percentage occurrence across 10 modelling runs on random partitions of training and test data

Term	Occurrence (%)	Component 1 (univariate)	Component 2 (bivariate)	Component 3 (trivariate)	Likelihood of initiation
1	100	CA = High			Likely
2	100	LAF = High			Likely
3	60	LAF = High	d_{mean} = High		Likely
4	80	O.Ang = Low	C.Ang = Low		Likely
5	80	O.Ang = Low	N.N.Ang = Low	d_{mean} = High	Unlikely

particles initiating fatigue for a range of simulated particle distributions and hence is a practical tool for fatigue optimisation studies.

Fatigue initiation at second phase particles has been the subject of considerable research in previous years, particularly in the MMC community. Complex stress fields arise around the second phase particles due to the mismatch in compliance between them and the surrounding matrix. Nutt and Needleman [9] first hypothesised that interfacial decohesion and hence crack initiation occur when the normal stress across the interface reaches a critical value. In later publications by the same authors, it is assumed that cavitation will occur when the hydrostatic component of the matrix stress state reaches a critical value [10,11]. This second hypothesis was confirmed by Whitehouse and Clyne [12], who experimentally observed that void nucleation sites along a particle interface correspond to points where the maximum hydro-

Table 3
Al–20Sn SUPANOVA terms selected and their percentage occurrence across 10 modelling runs on random partition of training and test data

Term	Occurrence (%)	Component 1 (univariate)	Component 2 (bivariate)	Likelihood of Initiation
1	70	OA = High		Likely
2	50	C.Asp.Rat = High		Unlikely
3	70	C.Ang = High		Unlikely
4	70	O.Ang = High	O.Asp.Rat = High	Likely
5	50	O.Ang = High	LAF = High	Likely
6	50	OA = High	N.N.Ang = High	Likely
7	60	LAF = High	N.N.Ang = High	Likely
8	60	C.Ang = High	N.N.Ang = High	Likely
9	60	C.Ang = High	d_{mean} = High	Likely
10	80	O.Ang = High	N.N.Ang = High	Unlikely

static stress is generated. This approach was then applied successfully by Gall et al. [13] to explain the initiation behaviour in Al–Si alloys.

In Al–12Sn–4Si, the probability of a low compliance Si particle causing fatigue initiation is seen to increase when the particle is large and its major axis is aligned parallel to the tensile axis. These results are in line with the findings of other workers. Whilst the FE analysis of Gall et al. [13] asserts that relative particle size has a negligible effect on the debonding of Si particles, they acknowledge that experimentally, Si size appears important. Dighe and Gokhale [14] reported that larger Si phases show an enhanced propensity for decohesion, and it is believed that this is linked to a greater probability that a larger particle will contain an interface flaw promoting decohesion [15]. The orientation effect may be explained with reference to the work of Gall et al. [13], who showed that given an elliptical particle the magnitude of the matrix hydrostatic stress was inversely proportional to the radius of curvature presented to the tensile axis, as shown in Fig. 11. Therefore, when the particle's major axis is aligned with the tensile axis (parallel), a small radius of curvature is presented to the tensile axis and hence the evolved hydrostatic stress is at maximum.

In contrast, Al–20Sn may be viewed as essentially the opposite to Al–12Sn–4Si, in that the included Sn particle has a higher compliance than the surrounding matrix. Therefore, as shown in Fig. 11, the points of maximum matrix hydrostatic stress will occur perpendicular to the tensile stress axis. The ANM results for Al–20Sn predict that fatigue crack initiation is likely in particles with high O.Ang (aligned perpendicular to the tensile axis) and high aspect ratio. Both of these are characteristics which will reduce the radius of curvature of the particle at the points of maximum hydrostatic stress, which, as shown by Gall et al. [13], will lead to this stress and hence the likelihood of decohesion being increased. In both alloys, the particles most likely to cause crack initiation appear to be relatively unclustered. Under these conditions, the influence of the nearest neighbour may be more significant. Hence, further FE studies of specific particle arrangements are ongoing for both systems to further elucidate the micromechanics in operation.

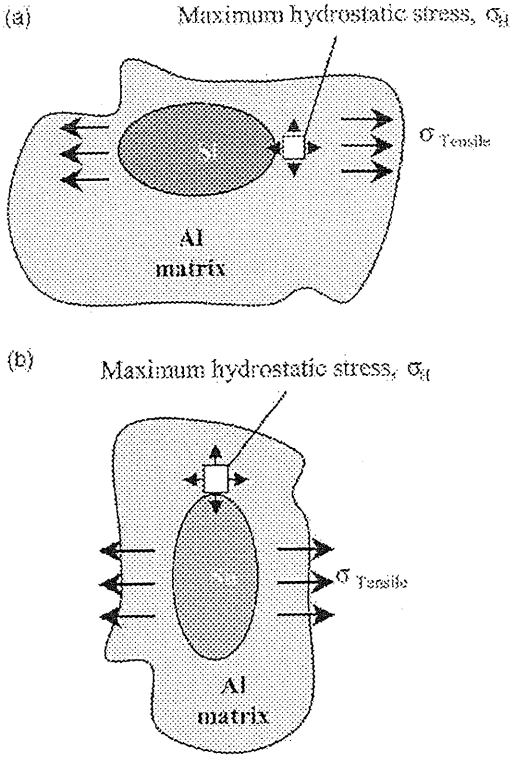

Fig. 11. Particles aligned for preferential initiation, showing positions of maximum hydrostatic stress in (a) Al–12Sn–4Si and (b) Al–20Sn.

It should be remembered that the Sn distribution in the Al–20Sn alloy will have a particular range of angles to the tensile axis due to the rolling directionality introduced during manufacture. As such, the choice of Al–20Sn bearing orientation within the rolled strip may be an important factor in fatigue initiation, whereas the Si in the Al–12Sn–4Si is effectively spheroidal, implying a lesser influence of its angular parameters on initiation. In the Al–20Sn tests reported here, the rolling direction

was perpendicular to the tensile axis. Preliminary tests on Al–20Sn flat strip specimens with the rolling direction oriented parallel to the tensile axis have exhibited improved fatigue lifetimes compared to perpendicularly oriented specimens—more detailed analysis of the initiation behaviour in these preliminary tests is currently ongoing.

6. Conclusions

Fatigue crack initiation in both materials occurs via decohesion of second phase particles from the surrounding matrix, and is therefore highly sensitive to local microgeometry. Microstructural tessellation allowed comparison between the particles associated with initiation and the background population. Whilst some univariate trends are obvious, it is difficult to elucidate more complex relations by inspection; hence, a SUPANOVA approach was applied. This showed that initiating Si particles in Al–12Sn–4Si are generally larger; with reference to the literature, this is attributed to a greater probability of an interfacial flaw around a larger particle. It was found that in Al–12Sn–4Si, a Si particle was more likely to cause initiation if its long axis was aligned with the tensile axis. Conversely, in Al–20Sn, initiation is more favourable when the Sn particle is aligned perpendicular to the tensile axis. However, due to the respective differences in compliance between the second phase particles relative to the matrix, and with reference to the work of Gall et al. [8], it can be shown that in both cases these preferential orientations will serve to maximise the hydrostatic stress around the particle. The overall secondary phase population only showed strong directionality in Al–20Sn, the Sn having been strung out during rolling, rather than broken and spheroidised like the Si in Al–12Sn–4Si. Preliminary testing has indicated that the fatigue performance of Al–20Sn may be increased by aligning the sample so that the majority of the Sn phase is in an orientation non-favourable for fatigue crack initiation. Further work on this phenomenon, together with the FE investigation of particle clustering and near neighbour orientation effects, is ongoing.

Acknowledgements

Support for this work from the School of Engineering Sciences, EPSRC (Grant no: GR/M13879) and Dana Glacier Vandervell is gratefully acknowledged. Presentation of this work was enabled by the kind support of the Armourers and Brasiers' Company and Corus.

References

[1] Gyde N. Fatigue fracture in babbit lined journal bearings. PhD thesis, Technical University of Denmark, Copanhagen, 1969.
[2] Shenton P, Perrin C. Private communication, Dana Glacier Vandervell.
[3] Joyce MR. Fatigue of aluminium linings in plain automotive bearings, Appendix 1. PhD thesis, University of Southampton, UK, 2001.
[4] Joyce MR, Syngellakis S, Reed PAS. Microstructural influences on fatigue crack initiation and early growth behaviour in plain bearing Al-based linings. In: Starke EA, Sanders TH, Cassada WA, editors. Proceedings of the ICAA-7. Aluminium alloys: their physical and mechanical properties. Mater Sci Forum 2000;331–7.
[5] Boselli J, Pitcher PD, Gregson PJ, Sinclair I. J Microsc 1999;195:104–12.
[6] Gunn S, Brown M. In: Proceedings of the IEEE International Workshop on Neural Networks for Signal Processing, Madison, WI, 1999.
[7] Reed PAS, Thomson RC, James JS, Putman DC, Lee KK, Gunn SR. Mater Sci Eng 2003;A346: 273–86.
[8] Lee KK, Harris CJ, Gunn SR, Reed PAS. In: Proceedings of the IJCNN, Washington, DC, USA, 2001. p. 2410–5.
[9] Nutt SR, Needleman A. Scripta Metall 1987;21:705–10.
[10] Llorca J, Needleman A, Suresh S. Acta Metall 1991;39:2317–35.
[11] Christman T, Needleman A, Suresh S. Acta Metall 1991;37:3029–50.
[12] Whitehouse AF, Clyne TW. Acta Metall 1995;43:2107–14.
[13] Gall K, Horstmeyer M, McDowell DL, Fan J. Mech Mater 2000;32:277–301.
[14] Dighe MD, Gokhale AM. Scripta Metall 1997;37:1435–40.
[15] Cox TB, Low JR. Metall Trans 1974;5:1457–70.